OPEN ACCESS
IOP Publishing
Journal of Physics D: Applied Physics
J. Phys. D: Appl. Phys. **50** (2017) 433002 (13pp)
https://doi.org/10.1088/1361-6463/aa865e

Topical Review

X-ray diffraction analysis of cubic zincblende III-nitrides

Martin Frentrup, Lok Yi Lee, Suman-Lata Sahonta, Menno J Kappers, Fabien Massabuau, Priti Gupta, Rachel A Oliver, Colin J Humphreys and David J Wallis

Department of Materials Science and Metallurgy, University of Cambridge, 27 Charles Babbage Road, Cambridge CB3 0FS, United Kingdom

E-mail: mf562@cam.ac.uk

Received 23 June 2017, revised 14 August 2017
Accepted for publication 15 August 2017
Published 26 September 2017

Abstract

Solving the green gap problem is a key challenge for the development of future LED-based light systems. A promising approach to achieve higher LED efficiencies in the green spectral region is the growth of III-nitrides in the cubic zincblende phase. However, the metastability of zincblende GaN along with the crystal growth process often lead to a phase mixture with the wurtzite phase, high mosaicity, high densities of extended defects and point defects, and strain, which can all impair the performance of light emitting devices. X-ray diffraction (XRD) is the main characterization technique to analyze these device-relevant structural properties, as it is very cheap in comparison to other techniques and enables fast feedback times. In this review, we will describe and apply various XRD techniques to identify the phase purity in predominantly zincblende GaN thin films, to analyze their mosaicity, strain state, and wafer curvature. The different techniques will be illustrated on samples grown by metalorganic vapor phase epitaxy on pieces of 4″ SiC/Si wafers. We will discuss possible issues, which may arise during experimentation, and provide a critical view on the common theories.

Keywords: x-ray diffraction, cubic GaN, gallium nitride, phase analysis

(Some figures may appear in colour only in the online journal)

1. Introduction

The group-III nitride semiconductors have a wide range of optoelectronic applications such as multiple quantum well (MQW) light emitting diodes (LEDs) and laser diodes emitting in the blue and green spectral region. Such devices are commonly grown along the *c*-direction of the hexagonal wurtzite phase. In this direction, strong internal electric polarization fields across the quantum wells (QWs) result in a reduction of the radiative recombination rates, and current density-dependent emission wavelength [1–3]. Although these effects are somewhat mitigated by the use of thin QW layers (typically 2–4 nm thick), long radiative recombination lifetimes and relatively low internal quantum efficiencies are observed for green light emitting structures [4, 5]. QW structures grown along non-polar axes of the wurtzite GaN phase, e.g. the *a*-plane and *m*-plane have been designed to avoid the polarization fields and related limitations. Although the non-polar wurtzite devices show very short radiative lifetimes [6, 7] and wavelength characteristics independent of current density [8], their quantum efficiencies have never surpassed those of the polar *c*-plane structures [7]. A possible explanation for the underachievement of green-emitting non-polar wurtzite devices could be the fact that indium-richer QWs

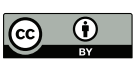

are required to achieve green emission, in the absence of the polarization field-related quantum confined Stark effect [2]. Apart from the increased interfacial strain of the InGaN QWs with the GaN buffer and barrier layers, the lower indium incorporation efficiency of non-polar growth planes compared to the polar growth plane requires low process temperatures for indium-rich layer growth [9]. This potentially results in high densities of impurities and point defects, which may act as non-radiative recombination centres and further decrease the efficiency of non-polar wurtzite MQWs [10]. Hence, GaN-related structures in the cubic zincblende phase have re-emerged as a promising approach to achieving improved efficiencies for green-wavelength LEDs after strong initial interest in the early-1990s and having been virtually abandoned in the early 2000s.

Cubic zincblende InGaN/GaN MQW structures grown on the $(0\,0\,1)_{zb}$ plane may be polarisation field free, as in the zincblende phase these fields are only induced by shear stresses [11], which are not present in $(0\,0\,1)_{zb}$ oriented films. Therefore, compared with *c*-plane hexagonal structures, the electron–hole wavefunction overlap is increased, which should lead to an increase in the radiative recombination rate. Furthermore, InGaN has a narrower bandgap in the cubic phase than in the hexagonal phase for a given indium content [12, 13], allowing green-wavelength emission to be achieved at lower indium contents than in non-polar wurtzite structures. However, as zincblende GaN and InGaN are metastable under most growth conditions, it is very likely that zincblende films will contain inclusions of the more stable wurtzite polytype, and also form wurtzite-like stacking faults (SFs) and lamellae [14–17]. In order to achieve single phase epitaxial films with reasonable crystal quality, it is necessary to support the growth process by a powerful structural characterization technique.

X-ray diffraction (XRD) is a highly appropriate method for this purpose, as it is non-destructive, well established and quickly provides detailed information on the structural properties of crystalline materials. However, most of the review manuals and technical reports on III-nitrides XRD characterization are centered on the hexagonal wurtzite form, while the cubic zincblende form is rarely discussed in any detail. Here we will focus on the XRD techniques specifically required for the analysis of cubic zincblende GaN and offering useful hints as well as material parameters for the experimentalist. Not only do we account for texture analysis and mosaicity quantification—both big topics in the field—we also discuss strain, strain anisotropy and its origin. These concepts are important for the development of large area zincblende GaN templates, where wafer bowing also comes into play. We will demonstrate the presented techniques on epitaxial GaN thin films grown on low cost, large area cubic $(0\,0\,1)_{zb}$ 3C-SiC/Si templates in order to give fast feedback for further growth optimization.

2. Crystallographic properties of III-nitrides

The group-III nitride materials—AlN, GaN, InN, and their alloys—can crystallize in the wurtzite, zincblende, and rock-salt structures, of which the first two are the most commonly observed phases in epitaxial thin films [11, 18]. The hexagonal wurtzite phase and cubic zincblende phase of GaN-based semiconductors are two different polytypes of the same material. As shown in figure 1, in both structures the bonds between the metal ions and the nitrogen ions are tetrahedrally coordinated, and the inter-ionic distances within the close packed planes are approximately the same. The two structures mainly differ in the stacking sequence of these planes, which in the wurtzite structure is …AaBbAaBbAaBb… for $(0\,0\,0\,1)_{wz}$ planes, while in the zincblende structure it is …AaBbCcAaBbCc… for $(1\,1\,1)_{zb}$ planes, where Aa, Bb, and Cc denote different metal-N bilayers.

The distance between crystal planes in the wurtzite structure is given by [19]

$$\frac{1}{d_{h\,k\,l}^2} = \frac{4}{3}\left(\frac{h^2+hk+k^2}{a^2}\right) + \frac{l^2}{c^2}, \tag{1}$$

and in the zincblende structure by [19]

$$\frac{1}{d_{h\,k\,l}^2} = \frac{h^2+k^2+l^2}{a^2}. \tag{2}$$

Here a and c are the individual lattice parameters of each structure, and h, k, and l are the Miller-Bravais-indices of the crystal plane. The crystallographic similarities of both polytypes, and the fact that the formation energy for both phases is similar [20], make it possible that fractions of both polytypes form during the growth process resulting in imperfect material.

3. Basics of XRD

XRD is one of the most frequently used methods for the characterization of crystalline samples. The method is based on the measurement of x-ray reflections, whose pattern represents a Fourier-transformed image of the crystal structure in reciprocal space. The diffraction angle $(2\theta_{hkl})$ of the $h\,k\,l$ reflection and the spacing d_{hkl} of $(h\,k\,l)$ planes in the crystal are related to each other via Bragg's law [21, 22]

$$2d_{h\,k\,l} \times \sin\theta_{h\,k\,l} = \lambda. \tag{3}$$

In reciprocal space the position of a reflection is described by its scattering vector $\mathbf{Q}$, with magnitude

$$|\mathbf{Q}| = \sqrt{Q_x^2 + Q_z^2} = \frac{4\pi}{\lambda} \times \sin\theta. \tag{4}$$

Here Q_x and Q_z denote the components of $\mathbf{Q}$ parallel and normal to the sample surface.

For the x-ray characterization of our cubic zincblende GaN thin films, we used two different standard laboratory diffractometers with Cu-Kα_1 sources ($\lambda = 1.540\,56$ Å). High-resolution measurements were performed on a Philips X'Pert diffractometer, in which the radiation from the x-ray tube was filtered by an asymmetric 4-crystal Bartels monochromator. Thereafter, an adjustable crossed slits collimator further shrank the beam in size and reduced the divergence to a few arc-seconds. As illustrated in figure 2, the incident beam then hit the sample at the incident angle ω. X-rays scattered by 2θ from the sample were then measured with a gas-proportional

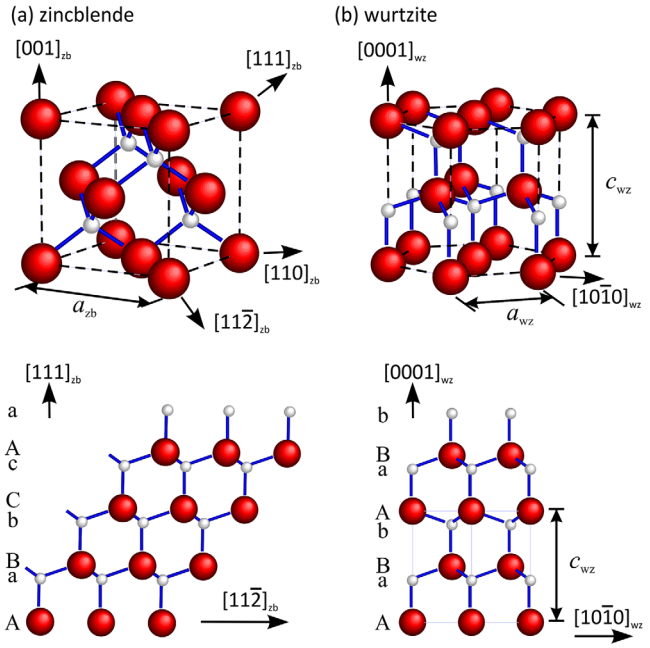

Figure 1. Crystal structure of zincblende (a) and wurtzite (b) GaN. The projections show the different stacking sequences of the close packed planes of Ga (red) and N (white) atoms.

point detector either directly (open detector configuration) or after passing through an additional monochromator (triple axis configuration) for high-resolution analysis. The samples were mounted on an Eulerian cradle, which allows rotation about the sample normal (ϕ), as well as tilt of the sample with respect to the beam-path-plane (χ). By changing the x- and y-position of the sample stage and reducing the beam size, different regions on the sample were illuminated and could be analyzed.

Reciprocal space maps were measured with a PANalytical Empyrean diffractometer equipped with a 2-bounce hybrid monochromator, 1/4°-slit, Eulerian cradle, and a PIXcel solid-state area detector in static line mode (1D). This configuration guarantees high intensity, and allows very fast and precise measurement of large maps in reciprocal space.

A correct alignment is an important factor for the accurate evaluation of the Bragg reflections and lattice properties. Therefore the goniometer 2θ-angle was calibrated on the primary beam before each measurement session. Then the sample was moved into the primary beam path (z-movement) until half of the intensity was blocked, following the best-practice approach suggested in [23].

The measurements were performed on predominantly zincblende GaN thin films, of which some of them contain wurtzite type GaN inclusions. The thin films were grown by metalorganic vapor phase epitaxy (MOVPE) on pieces of 4″ $(0\,0\,1)_{zb}$ cubic 3C-SiC templates deposited on (0 0 1) Si substrates. In order to relieve strain in the large area templates, the 3 μm to 8 μm thick SiC layers were etch-patterned with a polycrystalline square grid to create millimeter-length mesa structures. Lead tape can be used to mask these areas, so that they do not contribute to the XRD signal. The GaN samples used as examples here were randomly picked from various growth series of our ongoing MOVPE growth campaigns.

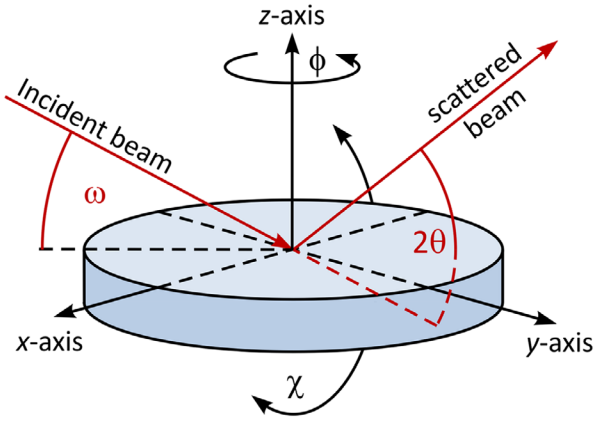

Figure 2. Illustration of the beam path and the different goniometer motions.

4. Texture analysis

4.1. Polytype identification

The phases and orientations present in a GaN thin film can be identified by XRD texture analyses, where one uses the different selection rules for the appearance of a reflection in both the zincblende phase and the wurtzite phase. While for some diffraction angles 2θ, reflections from both phases are superimposed; there are other, particularly suitable diffraction angles for which reflections from only one of the two phases are observable at once. For example, the wurtzite $0\,0\,0\,2_{wz}$ and zincblende $1\,1\,1_{zb}$ reflections, which both occur for $2\theta \approx 34.5°$ are unsuitable, as are the wurtzite $1\,1\,\bar{2}\,0_{wz}$ and the zincblende $2\,2\,0_{zb}$ reflections ($2\theta \approx 57.8°$). Herres *et al* proposed the use of the cubic $2\,0\,0_{zb}$ ($2\theta \approx 40.0°$) and the hexagonal $1\,0\,\bar{1}\,2_{wz}$ ($2\theta \approx 48.1°$) reflections for predominantly $(1\,1\,1)_{zb}$ and $(0\,0\,0\,1)_{wz}$ oriented films respectively, which has been shown to give reasonable results [24]. However, for predominantly $(0\,0\,1)_{zb}$ oriented cubic films one should rather use different zincblende reflections, as the reflections from the $\{1\,0\,0\}_{zb}$ side facets are often very weak and superimposed with surface scattering effects, making the identification of the in-plane epitaxial relations of the films difficult. There are several other suitable reflection combinations, which we have used for texture analysis: for example, the $1\,1\,3_{zb}$ reflections ($2\theta \approx 68.9°$) and $1\,\bar{1}\,0\,3_{wz}$ ($2\theta \approx 63.4°$), as they are well separated in reciprocal space and as the characteristic diffraction patterns are relatively simple to interpret.

4.2. Texture mapping

For XRD texture analysis, the angular distribution of selected reflections in reciprocal space is measured by mapping the surface of a hemisphere with the radius given by the particular Bragg condition (see figure 3). For this purpose, the sample is rotated around its surface normal (ϕ-scan), and stepwise tilted towards the beam path plane (χ-steps) after each scan. The measured intensities are visualized as a polar projection (radius = χ) or as a stereographic projection (radius = tan (χ/2)). In such a so-called pole figure, the center represents the direction of the surface normal, while poles at the edge

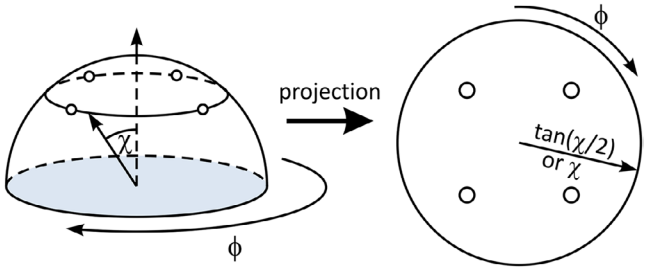

Figure 3. Diagram explaining the measurement geometry to map a texture in reciprocal space and its projection onto a 2D map.

of the plot ($\chi = 90°$) represent directions within the surface plane. Note that the use of a line focus for the primary beam rather than a spot focus may lead to an additional spread in χ of the normally round reflections.

To determine the phase purity, the main orientation and the crystallographic relation between different textures of the nitride film, the measurement of at least two texture maps is necessary—one for each phase. Figure 4 shows the texture maps collected at $2\theta \approx 34.5°$ (a), $2\theta \approx 68.9°$ (b), and $2\theta \approx 63.4°$ (c) of a GaN epilayer grown on a 3C-SiC/Si template under non-optimized conditions. In figure 4(a) four intense reflections at $\chi \approx 57°$ are clearly visible. As seen from the four-fold symmetry these reflections probably represent the $1\,1\,1_{zb}$ reflections of the zincblende phase. However, this result alone does not prove the absence of the wurtzite phase. The measured reflections can also represent the $0\,0\,0\,2_{wz}$ peaks originating from four different twins of the hexagonal wurtzite component growing on $\{1\,1\,1\}_{zb}$ facets of 3C-SiC, even if no cubic phase is present at all. In the more likely case that a mixture of the two phases has been grown, there will be contributions to the measured reflections from both phases.

To examine this further, we measured the distribution of the zincblende $1\,1\,3_{zb}$ reflections (figure 4(b)) and the wurtzite $1\,\bar{1}\,0\,3_{wz}$ reflections (figure 4(c)), which do not overlap with reflections of the other phase. The pattern of the $1\,1\,3_{zb}$ reflections show a four-fold symmetry, in which three reflections (two at $\chi \approx 72°$, and one at $\chi \approx 25°$) are arranged about a common $1\,1\,1_{zb}$ pole (compare with figure 4(a)). This confirms categorically that the main orientation of the cubic film is $(0\,0\,1)_{zb}$, which is equivalent to the SiC/Si template orientation, represented by the weak 0 0 4 Si reflection in the center of the pole-figure. In figure 4(c) the $\{1\,\bar{1}\,1\,0\,3\}_{wz}$ planes of the wurtzite phase cause a number of reflections, which form distorted hexagonal patterns around their common central 0 0 0 1 pole (not visible). The result indicates that the hexagonal wurtzite phase is present in the GaN film too, but that it is the minority phase, resulting in much weaker reflection intensities in comparison to the cubic zincblende reflections.

The phase purity of the GaN mixture can be qualitatively estimated by integrating the intensities of the reflections of each phase, and determining the ratio of these values. This might be sufficient to give fast feedback for optimization purposes in a crystal growth campaign, as suggested by [24]. However, for a more accurate quantification of the volume fraction of zincblende and wurtzite GaN phases, an additional correction is needed to take the different scattering efficiencies of both structures and their crystal planes into account. Since the zincblende and wurtzite phases have the same absorption coefficient, it is sufficient to consider only the different structure factors F_{hkl}, the volumes of the unit cells V_{uc}, and a geometric correction known as the Lorentz-polarization (LP) factor. Ignoring smaller correction factors, such as absorption correction and temperature correction, the integrated intensity of a single reflection $h\,k\,l$ is proportional to the materials volume amount V_{phase}, given by [25]:

$$I_{h\,k\,l} \propto \mathrm{LP} \times \left(\frac{|F_{h\,k\,l}|}{V_{\mathrm{uc}}}\right)^2 \times V_{\mathrm{phase}}, \tag{5}$$

with the Lorentz-polarisation factor [25, 26]

$$\mathrm{LP} = \frac{1 + \cos^2(2\theta)}{2 \times \sin(\theta) \times \cos(\theta)} \times \psi, \tag{6}$$

and the structure factor [25]

$$F_{h\,k\,l} = \sum_j f_j \times \mathrm{e}^{2\pi i(hx_j + ky_j + lz_j)}. \tag{7}$$

The factor ψ depends on the diffraction angle for powder samples ($\psi = \sin^{-1}(\theta)$), while it is constant for single crystals [26]. The coordinates x_j, y_j, z_j are the positions of each atom in the unit cell and are listed in table 1. The atomic scattering factors f_j of Ga and N are proportional to the electron number per atom, but also have a complex dependence on the diffraction angle and wavelength. Details of the correlation are described in the literature [25, 27, 28] and in online databases [29, 30]. With these corrections the $\{1\,1\,3\}_{zb}$ and $\{1\,\bar{1}\,0\,3\}_{wz}$ reflections in figure 4 reveal a volume portion of around 69 vol% zincblende GaN in this sample. The detection precision under which we collect the data here is a few volume percent, and is mainly influenced by the large variation in integrated intensity for reflections in different crystal directions.

The crystallographic relation between the zincblende and the wurtzite phase can be obtained by combining the pole figures in figure 4, and is found to be $(1\,1\,1)_{zb} \parallel (0\,0\,0\,1)_{wz}$, with $[1\,1\,\bar{2}]_{zb} \parallel [\bar{1}\,0\,1\,0]_{wz}$ and $[\bar{1}\,1\,0]_{zb} \parallel [1\,\bar{2}\,1\,0]_{wz}$ for two of the four unequal $\{1\,1\,1\}_{zb}$ facets in zincblende GaN. This unit cell arrangement is illustrated in figure 4(d), and it is unsurprising since the closed-packed planes of each structure are parallel to each other and differ only in the stacking sequence. Other groups observed a similar arrangement of the two phases by XRD [12, 17, 31, 32] and transmission electron microscope measurements [14], and it was also found that the zincblende and wurtzite phases arrange as alternating zincblende–wurtzite–lamella [15, 16]. As our example in figure 4 indicates, $(0\,0\,0\,1)_{wz}$ wurtzite GaN is not necessarily formed with equal probability on each of the four inequivalent $\{1\,1\,1\}_{zb}$ facets. Depending on the template miscut angle and miscut direction, the growth of wurtzite-like inclusions may occur preferentially along certain directions.

In samples grown under optimized conditions to maximize the zincblende phase, the x-ray intensity in the expected positions of the wurtzite phase reflections is negligible, i.e. only slightly above the background noise level. In these cases, it is very likely that the signal originated not from diffraction

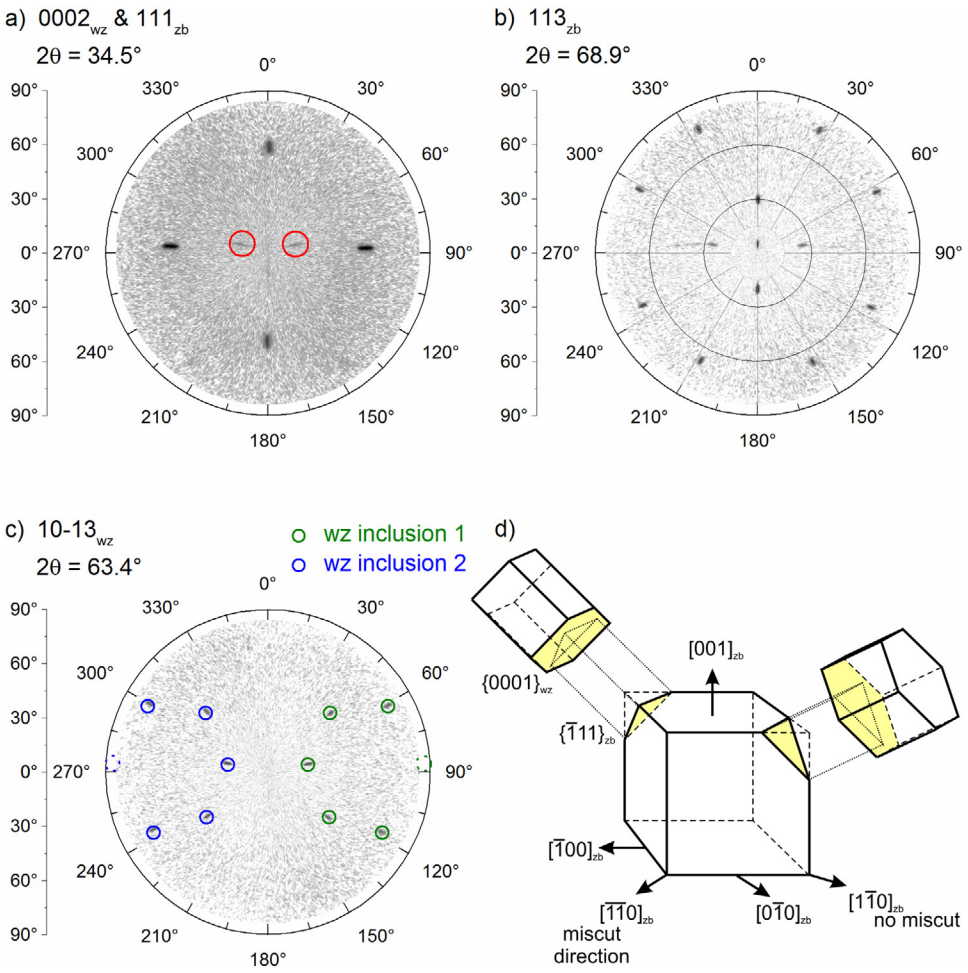

Figure 4. Pole figures for different wurtzite and zincblende reflections of GaN grown on $(0\,0\,1)_{zb}$ oriented 3C-SiC/Si-templates (a)–(c). The diagram illustrates the crystallographic arrangement of both phases.

by hexagonal wurtzite inclusions in the epilayers, but from diffuse scattering on planar defects, such as SFs. This can be proven by measuring a 2D reciprocal space map as described later in section 4.3.

Besides wurtzite inclusions, zincblende GaN thin films could also contain twinned zincblende regions. Similar to SFs, these are introduced by stacking errors of a single $(1\,1\,1)_{zb}$ plane, but in contrast to SFs, the zincblende matrix continues with a different stacking sequence …AaCcBbAaCcBb…. With respect to the surrounding GaN matrix, the cubic twins are tilted by approximately 70.4° around the $[1\,\bar{1}\,0]_{zb}$ axis, so that twin and matrix have the relation $(1\,1\,1)_{\mathrm{twin}} \parallel (1\,1\,5)_{\mathrm{matrix}}$ [32]. Such zincblende twins, and possibly twinned wurtzite-like material with a similar relation, cause the weak 1 1 1 reflections at $\chi \approx 15°$ (circled in figure 4(a)), and possibly at $\chi \approx 83°$ (out of range in figure 4(a)). Their volume portion is in the low percentage range.

4.3. Reciprocal space maps for texture analysis

2D reciprocal space maps (RSMs)—a combination of ω-2θ-scans or 2θ-scans with a stepwise change of the ω-angle after each scan—of suitable zincblende and wurtzite phase reflections can be used to analyze the phase purity of GaN samples, as well as several other structural properties. Suitable reflections include $0\,0\,2_{zb}$ and $1\,0\,\bar{1}\,1_{wz}$, as shown in figure 5 for two different samples with (a) and without (b) hexagonal inclusions. In both reciprocal space maps, the 0 0 2 reflections of zincblende GaN and 3C-SiC are clearly visible by their high intensities. The low-intensity streaks running along $\langle 1\,1\,1\rangle_{zb}$ through the $0\,0\,2_{zb}$ reflections are caused by diffuse scattering from $\{1\,1\,1\}_{zb}$ SFs in the structure, where diffracted x-rays suffer an additional phase shift between both sides of a SF. SFs may also lead to a small shift of the GaN reflections out of the ideal position. Another feature passing through the 3C-SiC reflection on a 2θ-arc is the detector streak (DS), caused by

Table 1. Position of the atoms in the ideal wurtzite and zincblende unit cell.

Ion	Wurtzite structure	Zincblende structure
Ga^{3+}	0, 0, 0 $^1/_3$, $^2/_3$, $^1/_2$	0, 0, 0; $^1/_2$, 0, $^1/_2$; $^1/_2$, $^1/_2$, 0; 0, $^1/_2$, $^1/_2$;
N^{3-}	0, 0, $^3/_8$; $^1/_3$, $^2/_3$, $^7/_8$;	$^3/_4$, $^3/_4$, $^3/_4$; $^1/_4$, $^3/_4$, $^1/_4$; $^1/_4$, $^1/_4$, $^3/_4$; $^3/_4$, $^1/_4$, $^1/_4$;

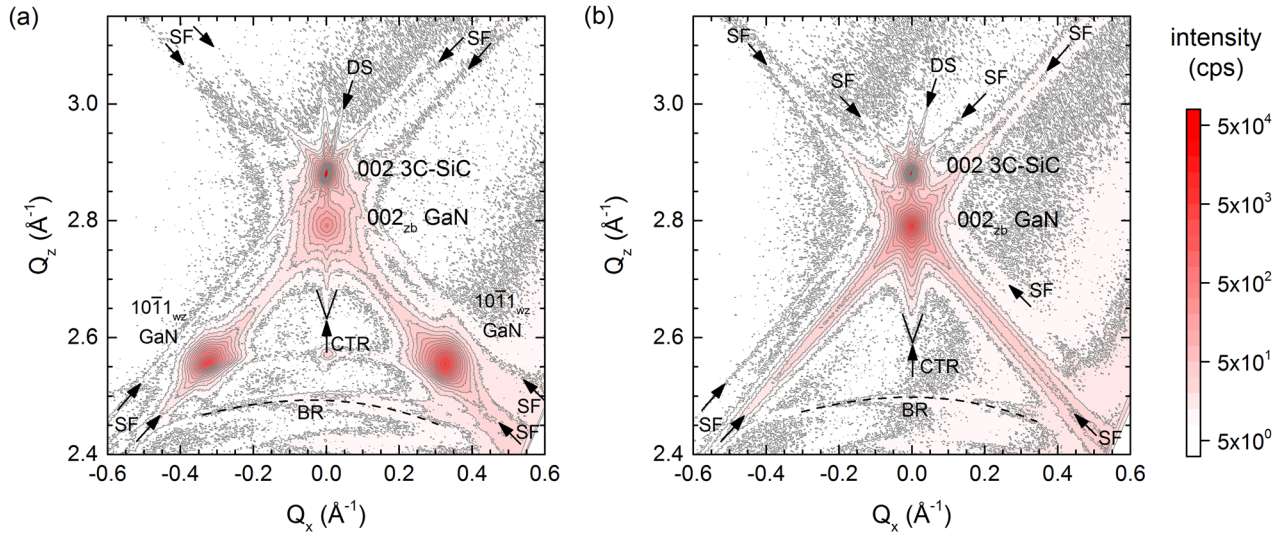

Figure 5. Measured RSMs of cubic GaN samples grown under (a) non-optimized conditions which promote hexagonal inclusion formation, and (b) optimized conditions, which gives close to 100% pure cubic GaN, with SF streaks, detector streak (DS), crystal truncation rod (CTR), and Bragg-ring (BR).

the instrument function of the diffractometer. The streak intersecting the $0\,0\,2_{zb}$ GaN reflection normal to the surface is the so-called (x-ray) crystal truncation rod (CTR), whose shape is influenced by the surface structures in agreement with observations from atomic force microscopy. The partially visible Bragg ring (BR) in the RSMs (with $2\theta \approx 35.6°$) stems from polycrystalline SiC deposited on the etched grid of the 3C-SiC/Si templates, and is related neither to the SiC mesa regions nor to the GaN epilayer. As the GaN epilayer is much thinner than the SiC template, similar Bragg rings from GaN grown on the etched grid are much weaker and often not visible. In the presence of wurtzite-like inclusions in the zincblende GaN thin film (figure 5(a)), two additional $1\,0\,\bar{1}\,1_{wz}$ reflections of the wurtzite GaN phase appear, which are absent in the sample without these inclusions (figure 5(b)). Since the SF streak overlaps with the wurtzite phase reflections, these streaks can be easily misinterpreted as a signal of small amounts of hexagonal inclusions in texture maps.

In comparison to the texture mapping (section 4.2), reciprocal space maps are much faster to perform even with high integration times by using a CCD detector (typically in 1D mode). This increases the signal-to-noise ratio, and hence allows the quantification of even relatively low proportions of wurtzite-like GaN inclusions (with equations (5)–(7)). However this method presumes a fixed epitaxial relation and provides no additional information on the presence of cubic twins. Furthermore, it can lead to misinterpretations when wurtzite inclusions are not formed on each of the $\{1\,1\,1\}_{zb}$ zincblende GaN facets, and thus may be missed in RSMs. For multi-phase films, we therefore recommend a combination of both methods.

5. Mosaicity and crystal defects

5.1. Mosaicity analysis

Due to the lack of suitable homo-substrates, cubic zincblende GaN-based nitrides are typically grown heteroepitaxially on foreign cubic substrates, such as GaAs [15, 17, 31–33], SiC [16, 34], Si [35], and various other cubic materials like GaP [36] and MgO [13]. The lattice mismatch between the different materials results in a high mosaicity and the formation of defects at grain boundaries in the epilayers. In general, mosaicity should be avoided as it negatively influences the physical properties of the sample, e.g. causes high electrical resistances at grain boundaries [37]. Hence, mosaicity needs to be quantified for crystal growth optimization.

In a simplified model originating from powder diffractometry, the thin film consists of mosaic blocks (grains), which differ slightly in their finite size and orientation relative to each other. The spread in size, tilt, and twist, together with microstrain and compositional inhomogenities (in the case of alloys) lead to broadening of the x-ray reflections in reciprocal space. Mosaic tilts lead to an angular broadening of reflections perpendicular to the surface, while twists result in an azimuthal spread around the surface normal. Hence for both the mosaic tilt and twist, the absolute broadening in reciprocal space $\Delta\mathbf{Q}_{hkl}$ increases linearly with the magnitude of the scattering vector $|\mathbf{Q}_{hkl}|$. The finite lateral size of mosaic grains causes a broadening parallel to the interface, being inversely proportional to the average real space size L and independent of the scattering vector magnitude ($\Delta|\mathbf{Q}_{hkl}| = 2\pi/L$). The effects of tilt, twist and finite grain size convolute to the spread of a reflection $h\,k\,l$ measured by ω-scans in skew-symmetry as follows [38]:

$$[\beta_{h\,k\,l}]^n = [\beta_{\text{tilt}} \times \cos\chi]^n + [\beta_{\text{twist}} \times \sin\chi]^n + \left[\frac{2\pi/L}{|\mathbf{Q}_{h\,k\,l}|}\right]^n. \quad (8)$$

Here β denotes the integrated breadth, and the exponent n takes values between 1 and 2 depending on the Gaussian η and Lorentzian $(1-\eta)$ contribution to a Pseudo-Voigt fit ($n = 1 + \eta^2$) (see appendix in [39]).

The measured peak broadening is then a combination of this mosaic broadening of the sample and the instrument function (measured without a sample). The latter one can be neglected

as long as it is much narrower than the mosaic broadening. Experimentally, the peak broadening effect due to the lateral size and tilt can be separated by measuring a series of ω-scans of different order symmetric reflections 00 l ($\chi = 0°$) and plotting $\beta^n_{h\,k\,l} \times |\mathbf{Q}_{hkl}|^n$ versus $|\mathbf{Q}_{hkl}|^n$ in a modified Williamson–Hall plot (not shown). The slope of the line (β^n_{tilt}) is related to the tilt component, and the ordinate offset $(2\pi/L)^n$ is related to the average grain size. Unfortunately, only the symmetric $0\,0\,2_{zb}$ and $0\,0\,4_{zb}$ zincblende GaN reflections are accessible with the commonly used Cu-Kα_1 radiation, which significantly limits the accuracy, especially of the finite size determination. Figure 6 shows the linear behavior of $\beta_{hkl} \times |\mathbf{Q}_{hkl}|$ in a traditional Williamson–Hall plot for which typically Lorentzian broadenings ($n = 1$ in equation (8)) are taken, even though Lorentzian profiles often do not fit very well to measured profiles. In comparison with the curve for Gaussian fits ($n = 2$), this results in a much larger value for the finite size L, as also pointed out by Lee *et al* [38]. As x-ray intensity profiles can be empirically described as a convolution of Gaussian and Lorentzian functions, the real lateral finite size is within these two extremes, depending on the portion of both the functions on the profile. Usually one gets the portions from the profile fitting, but they might vary for different reflections of a series. However, as the Lorentzian portion is often very small in such fits, mosaic block sizes estimated from pure Gaussian fits give a relatively good estimate.

The azimuthal spread around the surface normal due to mosaic twist can be determined from the off-axis reflections with large polar angles χ measured in screw-symmetric geometry. Ideally one would use one of the in-plane reflections ($\chi \approx 90°$), but those often exhibit very low intensities and are generally difficult to measure. For $(0\,0\,1)_{zb}$ oriented zincblende GaN films, the $3\,3\,1_{zb}$ reflection ($\chi \approx 76.7°$) may be better used instead. Alternatively, the integrated breadths of a series of different off-axis reflections, extracted from skew-symmetric ω-scans, can be extrapolated with equation (8) to determine the twist component.

Figure 7 shows such an extrapolation, for which we converted equation (8) to $\beta^n_{h\,k\,l} \times |\mathbf{Q}_{hkl}|^n$, and fitted this function (for $n = 2$) to the measured peak broadenings of an optimized cubic GaN sample by using the tilt and finite size values from the Williamson–Hall plot in figure 6. The circles mark the measured reflections, and the color code represents the extrapolated peak width in reciprocal space as a function of polar angle χ and scattering vector magnitude $|\mathbf{Q}_{hkl}|$. The dashed lines are contours of constant peak width. The profile at $\chi = 0°$ was already shown before (figure 6) and is only influenced by the tilt and the finite size of the mosaic blocks. With increasing polar angle χ, the broadening gradually increases, revealing a slightly higher mosaic twist ($\chi = 90°$) of 0.864° than tilt ($\chi = 0°$) of 0.755°. This trend is not much pronounced as tilt and twist are very similar, but it becomes more obvious for larger scattering vectors $|\mathbf{Q}_{hkl}|$ as the contribution of the finite size to the peak broadening decreases.

5.2. Threading dislocation densities measured by XRD

In general, mosaic tilt and twist are assumed to be associated with the formation of threading dislocations at grain boundaries in the thin film. Hence the XRD peak broadening is sometimes used to estimate the defect density in a thin film, by following different mosaic tilt models discussed in the literature. According to these models, the threading dislocation density D_{TD} in a well oriented mosaic film is proportional to $\beta_{\text{tilt/twist}}$ ([40, 41] as cited in [42], [43]),

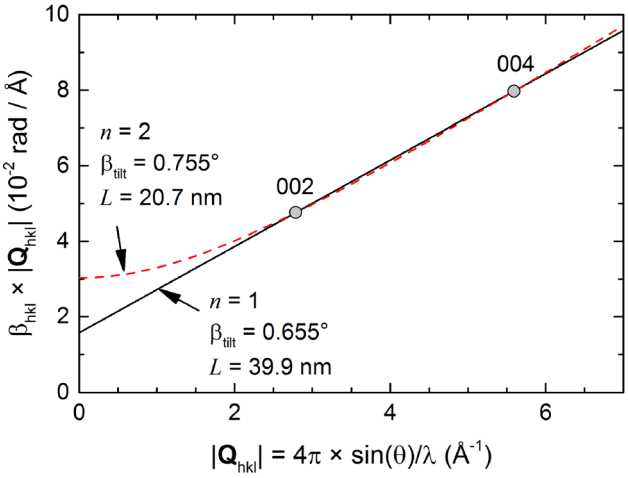

Figure 6. XRD peak width of an optimized zincblende GaN sample displayed in a traditional Williamson–Hall plot with fits for Lorentzian ($n = 1$) and Gaussian shape peaks ($n = 2$).

$$D_{\text{TD}} = \frac{\beta_{\text{tilt/twist}}}{\sqrt{(2\pi \times \ln 2)} \times \ |b_{\text{TD}}| \times L} \cong \frac{\beta_{\text{tilt/twist}}}{2.10 \times \ |b_{\text{TD}}| \times L} \tag{9}$$

while in poorly oriented films with randomly oriented grains and strictly statistically spread Burgers vectors and line vectors, the threading dislocation density is proportional to $\beta^2_{\text{tilt/twist}}$ [43]

$$D_{\text{TD}} = \frac{\beta^2_{\text{tilt/twist}}}{2\pi \ \times \ln 2 \times b^2_{\text{TD}}} \cong \frac{\beta^2_{\text{tilt/twist}}}{4.35 \times b^2_{\text{TD}}}. \tag{10}$$

Here the parameter L is the average lateral finite size of the grains, while b_{TD} denotes the Burgers vector of the dislocation with a value of $a_{zb}/\sqrt{2} \approx 3.189$ Å in the case of perfect dislocations in zincblende GaN.

In contrast to wurtzite GaN material, where the threading dislocation line vector propagates predominantly along the $[0\,0\,0\,1]_{wz}$ c-direction, the threading dislocations in zincblende GaN run along multiple $\langle 1\,1\,0\rangle_{zb}$ directions. Thus, the equations above do not allow separating between edge-type, mixed-type, or screw-type dislocations in zincblende GaN. However, it is well known that the dominating threading dislocation type in zincblende like structures are 60°-mixed-type perfect dislocations [44].

In an intensive comparative study using XRD and transmission electron microscopy (TEM) to estimate the defect densities in wurtzite GaN films, Metzger *et al* found a good match with the random distribution model (equation (10)), even though the assumptions of the model are not fulfilled at all in oriented epitaxial thin films. Contrary to expectations, the model for oriented mosaic films revealed threading dislocation densities which were more than a magnitude lower than the values estimated from TEM [42]. Lee *et al*

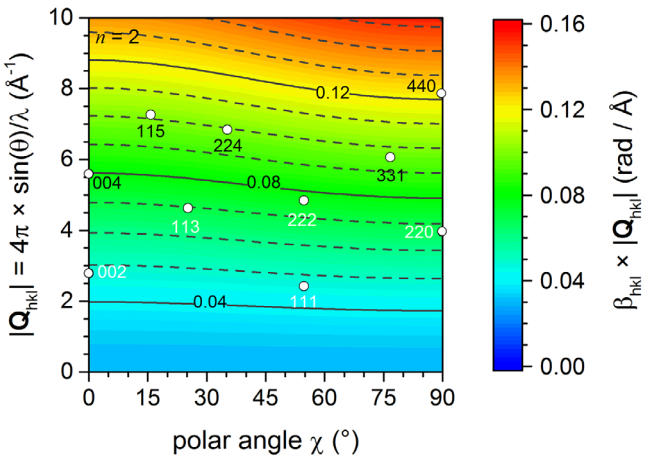

Figure 7. Extrapolated peak width $\beta_{hkl} \times |\mathbf{Q}_{hkl}|$ in reciprocal space (colour code) as a function of polar angle χ and scattering vector magnitude $|\mathbf{Q}_{hkl}|$ estimated from a series of skew-symmetric ω-scans. The circles show the position of the measured reflections, used for the extrapolation.

came to similar conclusions and noted that large differences in the measured dislocation densities between TEM and XRD are common [38]. In general, XRD seems to slightly overestimate the threading dislocation density when the twist component is used, and underestimate the density when the broadening due to tilt is used [38]. Furthermore, it should be noted that for very thin films, XRD also samples the tilts associated with misfit dislocations at the GaN/SiC interface. If the Burger's vectors of the dislocations are randomly oriented, the associated strain fields will tend to cancel out as the film thickness increases. However, if the Burger's vectors are not random the tilts can persist. This discussion shows that there are still some limitations on the current understanding of even the measurements of the more widely studied wurtzite GaN, and that defect densities estimated by XRD need be handled with care. This is especially the case when comparing samples of different layer thicknesses.

5.3. The influence of layer thickness

Typically the intensity spread of x-ray reflections is not constant but decreases with increasing film thickness, as shown in figure 8 by the full width at half maximum (FWHM) of the 002_{zb} zincblende GaN reflection in ω-scans. It is also evident that zincblende GaN grown on low lattice mismatch substrates, like 3C-SiC (3.4%) and MgO (7.0%), exhibits a lower mosaicity than similar thick cubic GaN films grown with a much larger mismatch on Si (−17.0%) or GaAs (−20.3%). Moreover, the figure shows that MOVPE-grown zincblende GaN (our data) compares well with state-of-the-art cubic GaN films grown by MBE [45, 46]. The decreasing intensity spread of the reflections with increasing film thickness is commonly associated with an overall reduction in the defect density and an improvement in the material quality for thicker epitaxial films. TEM investigations reveal a strong reduction in SF density with increasing layer thickness by reactions between pairs of SFs under formation of perfect edge dislocations or partial threading dislocation. Martinez-Guerrero *et al* observed a nearly exponential decay of the SF density from 5×10^6 cm^{-1} to 3×10^5 cm^{-1} in the first 500 nm of zincblende GaN growth [46]. In our MOVPE-grown cubic GaN films, the SF density reduces from 10^7 cm^{-1} directly at the template interface to 3×10^4 cm^{-1} close to the surface of 1200 nm thick films as revealed by TEM measurements [47]. However, the SF density affects foremost the shape and intensity profile along the SF-streak in reciprocal space (as shown in [48] for basal plane SFs in wurtzite GaN and in [49] for SFs in face-centered cubic (fcc) nano-crystals), but ω-scans of the symmetric 002_{zb} reflection have almost no overlap with the SF streak profile. Hence, the observed narrowing of the peak with increasing layer thickness, as shown in figure 8, cannot be directly related to the SF reduction.

Several reports in the literature suggest that the trend in figure 8 is due to a reduction in threading dislocation density with increasing film thickness, as a result of threading dislocation reaction, but TEM evidence for this assertion is scarce [45, 54–56]. Theoretical models predict that the threading dislocation density is inversely proportional to the film thickness t [57, 58]. Combining these models with the reflection broadening due to mosaicity reveals a decrease in the intensity spread by a factor of t^{-1} or $t^{-1/2}$, depending on whether a highly oriented thin film (equation (9)) or a powder sample (equation (10)) is assumed. As one can see from the dashed lines in figure 8, the experimental data do not follow the predicted trend. Instead the observed decay is much weaker, following approximately a $t^{-1/3}$ dependency. This may be explained by the generation of new threading dislocations, when SFs react with each other, and which to the best of our knowledge is not considered in the current models. Furthermore, one should consider that these models predict a threading dislocation density reduction after a certain thickness, while XRD is an integration method which provides a weighted average value over the whole layer thickness. It should also not be forgotten that there is a natural reduction in the width of the x-ray reflections with increasing layer thickness, as the number of scattering atoms increases. All this makes a comparison of the material quality of samples with different thickness difficult.

The arguments mentioned above do not exclude the reduction of threading dislocation density with increasing film thickness, but highlight the deficiencies between current models and the lack of experimental evidence. In particular, more TEM studies are needed to analyze the types of threading dislocations present and determine their densities as a function of layer thickness.

6. Material parameters for the strain analysis

The lattice parameters for zincblende III-nitrides are not yet well established experimentally, since such thin films suffer from stacking disorder, undoubtedly a high density of line defects, and wurtzite inclusions, resulting in local strain variations and relatively broad reflections. Furthermore, most of

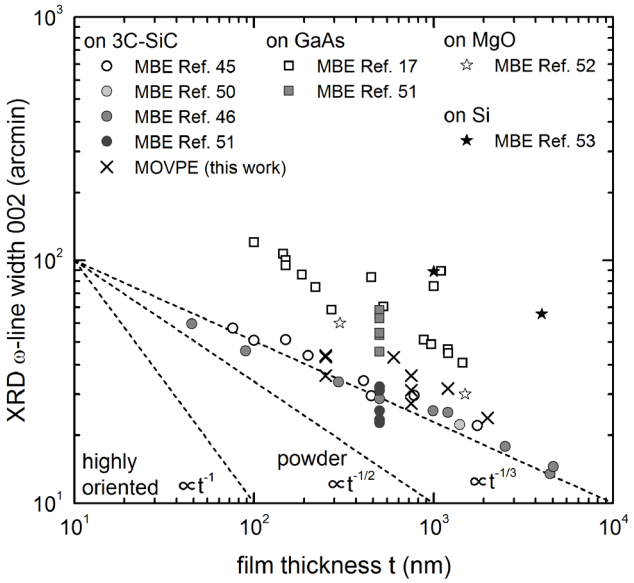

Figure 8. Decrease of the XRD ω-linewidth (FWHM) with increasing film thickness for oriented zincblende GaN grown on relevant substrates 3C-SiC, GaAs, MgO, and Si [17, 45, 46, 50–53].

the reported XRD experiments on predominantly zincblende GaN films are focused on phase purity analysis, rather than high-resolution lattice parameter measurements.

Our own measurements of the zincblende GaN lattice parameter using high-resolution 2θ-ω-scans of 8 on- and off-axis reflections and a least squares fit give a value of $(4.505\,97 \pm 0.000\,38)$ Å, which is in good agreement with experimental data in [61], and can be used as reference data for strain analyses in zincblende GaN thin films.

To the best of our knowledge, no experimentally determined accurate lattice parameters are mentioned in the literature for zincblende InN and AlN. In these cases, it is therefore necessary to derive the values from the well-established wurtzite lattice parameters a_{wz} and c_{wz}. However, in wurtzite-like III-nitrides strong internal electric fields lead to a distortion of the unit cell from the ideal shape, with a c_{wz}/a_{wz}-ratio of $\sqrt{8/3} \approx 1.633$. In reality, c_{wz} is typically smaller and a_{wz} slightly larger than in ideal case, and hence the estimated zincblende parameter of nominally unstrained III-nitrides can differ a lot, as one can see from the values in table 2. As a_{wz} is less affected by the wurtzite unit cell distortion than c_{wz}, this parameter gives reasonably good values for the natural lattice constant of the zincblende phase a_{zb}. Alternatively, the lattice parameters derived from the unit cell volumes ($a_{zb} = \sqrt[3]{V_{zb}} = \sqrt[3]{2V_{wz}}$) can be used. Presumably, the natural unstrained lattice constants of zincblende nitrides are somewhere between these theoretical values, and this assumption is in good agreement with the experimental data known so far.

Table 2 also contains the elastic constants C_{11} and C_{12} for the zincblende III-nitrides as stated in [62], and which can be used for stress and strain calculations as described in section 7.

7. Strain

During the growth of thin films on foreign substrates and during the heterostructure growth of alloys with different compositions, the films are subjected to varying stresses, which often result in an elastic deformation of the crystal lattice. Such lattice strains have a significant impact on the physical properties and the performance of semiconductor devices. Hence, the understanding and monitoring of these strains during device development are of high importance. In the following sections, we will discuss the different sources of strain, and describe how the strain in a thin zincblende GaN film can be measured.

7.1. Lattice mismatch strain

In epitaxial thin films, the lattice mismatch between the thin film and the underlying template produces biaxial in-plane strains, when the size of both lattices are forced to match each other. Three different states are commonly used to describe the thin film deformation. The thin film is fully strained when its lattice matches the dimensions of the template lattice at the common interface, while the film is fully relaxed when its lattice is undistorted and has its natural dimensions. The state between both extremes is called partially relaxed.

In reciprocal space, the lattice mismatch strain results in a shift of the reciprocal lattice points (RLPs) of the GaN thin film from their expected position and with respect to the RLPs of the substrate. The relative separation between layer and buffer peaks can be either measured in several individual ω-2θ-scans or more commonly by collecting a reciprocal space map in asymmetric geometry. The latter generally gives a better overview of the relationship between the x-ray reflections of the different layers, but a correction of the sample miscut by a second scan is required for the lattice mismatch strain evaluation. Moreover, one should take into account that the layer used as a reference may be affected by the substrate as well, which lowers the accuracy of this method. Ideally one should use a substrate peak as a reference, but there can be a large separation in reciprocal space for systems with a large mismatch.

The strain in a certain direction of the thin film is then given as follow:

$$\varepsilon_i = \frac{a_i - a_0}{a_0}, \tag{11}$$

where a_0 is its natural lattice constant, and a_i is the measured constant in the same direction. Due to the relatively low material quality often found in zincblende nitride materials there are currently no accurate reference values for the natural lattice parameter available in the literature, as discussed in the previous section. For GaN one can use the experimentally determined values we provided in section 6. For other group-III nitrides we recommend using the values which are derived from the wurtzite a-parameter or from the wurtzite cell volume (see table 2), as the wurtzite lattice parameters are well known.

Table 2. Lattice parameters and elastic constants of wurtzite and zincblende GaN, InN, and AlN.

Parameter	GaN	InN	AlN
wurtzite			
a_{wz} (Å)	3.189 40[a]	3.5446[b]	3.111 97[a]
c_{wz} (Å)	5.186 14[a]	5.7034[b]	4.980 89[a]
zincblende			
a_{zb} (Å)	4.4913[c]	4.9393[c]	4.3136[c]
	4.5105[d]	5.0128[d]	4.4010[d]
	4.5041[e]	4.9882[e]	4.3717[e]
	4.510 ± 0.005[f]	5.01 ± 0.01[g]	4.373 ± 0.002[h]
	$4.505\,97 \pm 0.000\,38$[i]	5.02 ± 0.005[j]	—
C_{11} (GPa)	293[k]	187[k]	304[k]
C_{12} (GPa)	159[k]	125[k]	160[k]

[a] Experiment [59].
[b] Experiment [60].
[c] Calculated from wurtzite parameters using $\sqrt{3}c_{wz}/2$.
[d] Calculated from wurtzite parameters using $\sqrt{2}a_{wz}$.
[e] Calculated from wurtzite parameters using $\sqrt[3]{2V_{wz}} = \sqrt[3]{\sqrt{3}c_{wz}a_{wz}^2}$.
[f] Experiment [61].
[g] Experiment [12].
[h] Experiment [54].
[i] Experiment (this work).
[j] Experiment [13].
[k] Recommended by [62].

Assuming that the thin film is stress-free in the growth direction (commonly labelled as z), the strain of a $(0\,0\,1)_{zb}$ oriented film in the growth direction is given via Hooke's law as [63]

$$\varepsilon_z = -\frac{C_{12}}{C_{11}} \times (\varepsilon_x + \varepsilon_y), \tag{12}$$

where ε_x and ε_y are the strains in the two in-plane directions, and C_{11} and C_{12} are the materials' elastic constants (see table 2). In the case of isotropic in-plane strain ($\varepsilon_x = \varepsilon_y$), this can be further simplified. The strain relations for orientations other than $(0\,0\,1)_{zb}$ differ from equation (12), and can be derived by coordinate transformation, as described in [63].

7.2. Thermal mismatch strain and growth induced strain

Small strain in an epitaxial thin film originates from the thermal mismatch between the used substrate and epilayer, or is formed in the early stage of growth. It is typically much smaller than strain due to lattice mismatch, but can be large compared to the residual mismatch strain in a partially relaxed film.

As GaN has a larger thermal expansion coefficient than SiC and Si [64–67], the remaining thermal strain after cooling down from the growth temperature leads to a tension in the GaN film at its interface with the substrate. For typical zincblende GaN growth temperatures in the range between 700 °C and 1000 °C, the theoretical thermal strain is in between 1.1×10^{-3} and 1.6×10^{-3} when a Si substrate is used.

Growth-induced strain occurs due to island coalescence during the nucleation on the substrate in the early stages of growth. Its magnitude is given by the smallest possible gap between two islands Δ and the average island size s_{island} in the particular in-plane direction [68]:

$$\varepsilon_{x,y} = \frac{\Delta}{s_{\text{island}}}. \tag{13}$$

In case of $(0\,0\,1)_{zb}$ orientated zincblende thinfilms Δ is given by the nearest neighbor distance at the interface $a_{zb}/\sqrt{2}$.

Relative lattice parameter measurements as described in section 7.1 are not sufficiently accurate to determine such small strains, as the resolution is often low and as the substrate itself may also be influenced by strain. Instead, analyses of very small strains require absolute measurement of the lattice parameters, using high-resolution 2θ-ω-scans of a larger set of different reflections. Then the as-measured plane spacings d_j are matched by the plane spacings of a model crystal d_{sim} using a least squares fit:

$$\sum_j W_j^2 \times \left(d_{\text{sim}}^{-2} - d_j^{-2}\right)^2 \to \min. \tag{14}$$

To increase the accuracy of the method a weighting factor W_j such as $2\theta_j/\Delta(2\theta_j)$ [69] or $d_j^{-2}/\Delta(d_j^{-2}) = 0.5 \times \tan(\theta_j)/\Delta(2\theta_j)$ (this work) is used, to take the imprecision of the measurement $\Delta(2\theta_j)$ into account.

Often it is necessary to choose a suitable coordinate system, which describes the geometry of the problem better than the natural lattice. The following example illustrates this. Table 3 lists 2θ values for different reflections, which were measured from a zincblende GaN film grown on a 3C-SiC/Si template with 4° miscut in $[1\,1\,0]_{zb}$ direction. The Bragg angles of all reflections $h\,h\,l$ tilted in the miscut direction are significantly smaller than the similar reflections $h\,\bar{h}\,l$ tilted perpendicular to the miscut, indicating a difference in the lattice dimensions for these two directions. In consequence, the natural crystal lattice is slightly sheared within the growth plane. This can be simplified by using a new coordinate system x', y', z' with x' (y') parallel (perpendicular) to the sample miscut, and z' pointing in the growth direction. The shearing in the natural lattice is then expressed in the new x', y', z' system by a small length difference between both in-plane lattice constants. Also note that by this coordinate transformation the new unit cell is $\sqrt{2} \times \sqrt{2} \times 1$ larger than the unit cell in the natural lattice. Using this approach, the least squares fit (equation (14)) together with Bragg's law (equation (3)) give a unit cell size of $x' = (6.395\,66 \pm 6.7 \times 10^{-4})$ Å, $y' = (6.384\,65 \pm 5.5 \times 10^{-4})$ Å, and $z' = (4.492\,36 \pm 3.2 \times 10^{-4})$ Å in the new coordinate system, and an anisotropy of the in-plane strain of $\varepsilon'_x = (3.65 \pm 0.11) \times 10^{-3}$ respectively $\varepsilon'_y = (1.92 \pm 0.09) \times 10^{-3}$.

It is known that a substrate miscut can lead to strain relaxation in epitaxial thin films via alignment of the threading dislocations [70–72], but then the zincblende GaN layer would be less strained in the miscut direction (ε'_x) than in the perpendicular direction (ε'_y). Since we observed the opposite case, we can rule out this relaxation mechanism for this sample. Instead, the results indicate that the strain anisotropy is probably due to the coalescence of islands with different size

Table 3. Reflections in the natural coordinate system (hkl) and rotated coordinate system ($h'k'l'$) of a zincblende GaN-sample, with 2θ and $\Delta(2\theta)$ derived from high-resolution 2θ-ω-scans.

Reflection hkl in nat. lattice	Reflection $h'k'l'$ in $x'y'z'$ lattice	Measured 2θ (°)	FWHM $\Delta(2\theta)$ (°)
002	002	40.0871	0.2452
004	004	86.6495	0.5002
$1\bar{1}3$	023	69.2284	0.3132
$2\bar{2}4$	044	114.0130	0.6891
$3\bar{3}1$	061	96.1246	0.4233
113	203	69.1963	0.3690
224	404	113.8499	0.7261
331	601	95.9402	0.5198

in the two in-plane directions, which has been observed in atomic force microscopy images [73].

8. Wafer curvature analysis

In heteroepitaxial thin films, stress above a certain level can be relieved by the formation of defects, or in the case of tensile surface stress by the formation of cracks. Moreover, the stress in the thin film can be lowered by bowing of the whole sample. This is often the case in thick, medium stressed epilayers, such as templates and buffer layers. Thermal strains can also lead to a significant wafer bowing. This is especially a problem with large area templates with diameters up to 8″, where even small bows lead to significant deviations in uniformity during growth and processing. Hence, control and management of strain and wafer bowing are of significant interest.

The bow of a wafer can be determined with XRD by measuring the incident beam angle ω_j for a symmetric reflection at different positions of the sample x_j. In bowed samples, the lattice planes are also curved with the bow of the wafer. In consequence, the incident angle needs to be corrected for different positions along the diameter of the wafer. Wafer curvature κ and radius of bow R are then given by the relative change of ω_j and x_j [74]:

$$\kappa = \frac{1}{R} = \frac{\tan(\Delta\omega)}{\Delta x} \approx \frac{\Delta\omega}{\Delta x} \qquad (15)$$

as illustrated by the schematic in figure 9. Since the reflections of the zincblende GaN thin film are often relatively broad, it is more suitable to use a narrower symmetric reflection of the underlying template. By using larger distances between the different measurement positions, and a beam mask to reduce the irradiated area on the sample surface, the resolution of the measurement can be further improved. Figure 9 shows such a curvature measurement for a 4″ 3C-SiC/Si template, where the 002 SiC reflection was used. The curvature of the wafer along the measured direction can be easily determined graphically by linear interpolation of the measured incident beam angles. A positive (negative) slope corresponds to a concave (convex) bow of the wafer. The example in figure 9 gives a convex bow of $\kappa = -51.5$ km^{-1} or $R = -19.4$ m. It should be noted however that this technique measures the curvature

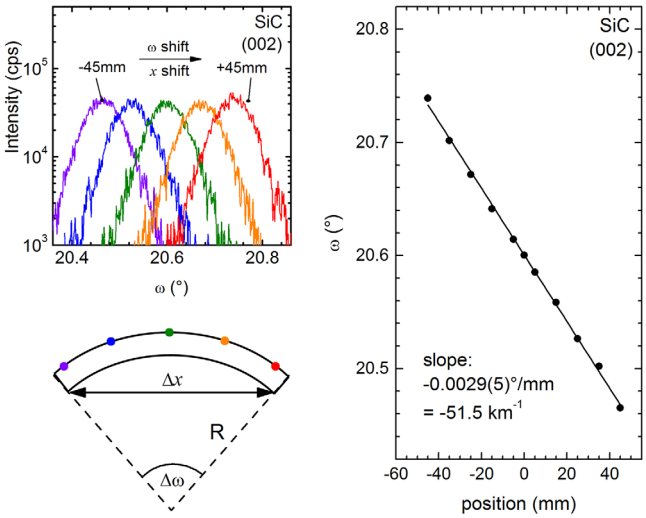

Figure 9. An example for an XRD wafer bow analysis of a 4″ 3C-SiC/Si template, revealing a convex curvature of -51.5 km^{-1}.

of the substrate planes. If the substrates already contain a high density of dislocations or a grain structure then the planes in the substrates may already be curved before the thin film growth and therefore the measured bow may not give an accurate reflection of the residual stress in the wafer. For this reason, there may also be discrepancies between the bow measured by x-ray and optical techniques. We find that for the high-quality templates used in these studies, the discrepancy between the curvature measured by XRD and optical techniques is negligibly small.

9. Conclusion

In this review, we have presented and discussed various XRD techniques to characterize the structural properties of epitaxially grown zincblende GaN thin films, including analysis of the phase purity, mosaicity, strain state, and wafer curvature. To identify the polytypes and orientations present in the GaN film, we proposed the use of a combination of texture mapping and reciprocal space maps. XRD ω-scans allow a rough characterization of the mosaicity in the film to give fast feedback in a growth optimization campaign, but values need to be taken with care when comparing samples of different thickness. Our examples show also that the material quality of large area MOVPE-grown zincblende GaN compares well with state-of-the-art cubic GaN films grown by MBE. This is quite promising for various possible industrial applications in the future. Furthermore, the lattice parameters and the elastic constants of AlN, GaN, and InN were provided as reference values for strain quantifications. High-resolution measurements of multiple reflections were used to estimate the lattice parameter of zincblende GaN with a high precision. To determine the curvature of large area wafers, we recommend to use the narrow symmetric reflections of the template rather than from the GaN layer and to use a mask to reduce the beam size on the wafer.

In summary, this review gives a detailed overview for academic and industrial researchers on the XRD characterization

of cubic zincblende III-nitride thin films and highlights some of the pitfalls that can lead to incorrect conclusions about the quality of zincblende GaN films.

Acknowledgment

We would like to thank Anvil Semiconductors Ltd. for providing 3C-SiC on Si templates for our experiments, and Innovate UK for financial support within the Energy Catalyst Round 2—Early Stage Feasibility scheme (Ref. 132135): 'To demonstrate the potential to make low cost, high efficiency LEDs using 3C-SiC substrates'. S-L Sahonta and M J Kappers would also like to acknowledge the support of EPSRC through platform grant no. EP/M010589/1: 'Beyond Blue: New Horizons in Nitrides'. D J Wallis would like to acknowledge the support of EPSRC through grant no. EP/N01202X/1. Datasets for the figures in this paper can be found at https://doi.org/10.17863/CAM.12450.

References

[1] Miller D A B, Chemla D S, Damen T C, Gossard A C, Wiegmann W, Wood T H and Burrus C A 1985 *Phys. Rev.* B **32** 1043–60
[2] Fiorentini V, Bernardini F, Della Sala F, Di Carlo A and Lugli P 1999 *Phys. Rev.* B **60** 8849–58
[3] Hammersley S, Kappers M J, Massabuau F C-P, Sahonta S-L, Dawson P, Oliver R A and Humphreys C J 2015 *Appl. Phys. Lett.* **107** 132106
[4] Nippert F, Karpov S Y, Callsen G, Galler B, Kure T, Nenstiel C, Wagner M R, Straßburg M, Lugauer H-J and Hoffmann A 2016 *Appl. Phys. Lett.* **109** 161103
[5] Hammersley S, Kappers M J, Massabuau F C-P, Sahonta S-L, Dawson P, Oliver R A and Humphreys C J 2016 *Phys. Status Solidi* c **13** 209–13
[6] Marcinkevičius S, Kelchner K M, Kuritzky L Y, Nakamura S, DenBaars S P and Speck J S 2013 *Appl. Phys. Lett.* **103** 111107
[7] Dawson P, Schulz S, Oliver R A, Kappers M J and Humphreys C J 2016 *J. Appl. Phys.* **119** 181505
[8] Detchprohm T, Zhu M, Li Y, Zhao Y L, You S, Wetzel C, Preble E A, Liu L, Paskova T and Hanser D 2010 *Appl. Phys. Lett.* **96** 051101
[9] Zhao Y *et al* 2012 *Appl. Phys. Lett.* **100** 201108
[10] Chichibu S F, Uedono A, Onuma T, Sota T, Haskell B A, DenBaars S P, Speck J S and Nakamura S 2005 *Appl. Phys. Lett.* **86** 021914
[11] Hanada T 2009 *Basic Properties of ZnO, GaN, and Related Materials. In Oxide and Nitride Semiconductors—Processing, Properties, and Applications* ed T Yao and S-K Hong (*Advances in Materials Research* vol 12) (Berlin: Springer) pp 1–19
[12] Schörmann J, As D J, Lischka K, Schley P, Goldhahn R, Li S F, Löffler W, Hetterich M and Kalt H 2006 *Appl. Phys. Lett.* **89** 261903
[13] Compeán García V D, Orozco Hinostroza I E, Escobosa Echavarría A, López Luna E, Rodríguez A G and Vidal M A 2015 *J. Cryst. Growth* **418** 120–5
[14] Trampert A, Brandt O and Ploog K H 1997 *Angew. Chem., Int. Ed. Engl.* **36** 2111–2
[15] Shen X M, Wang Y T, Zheng X H, Zhang B S, Chen J, Feng G and Yang H 2003 *J. Cryst. Growth* **254** 23–7
[16] Wu J, Yaguchi H, Nagasawa H, Yamaguchi Y, Onabe K, Shiraki Y and Ito R 1997 *Japan. J. Appl. Phys.* **36** 4241–5
[17] Yang H, Brandt O and Ploog K 1996 *Phys. Status Solidi* b **194** 109–20
[18] Ambacher O 1998 *J. Phys. D: Appl. Phys.* **31** 2653–710
[19] Cullity B D 1956 *Elements of X-Ray Diffraction* (Reading, MA: Addison-Wesley) Appendix 1 (A1-1) p 459
[20] Yeh C-Y, Lu Z W, Froyen S and Zunger A 1992 *Phys. Rev.* B **46** 10086–97
[21] Bragg W H 1915 Bakerian lecture: x-rays and crystal structure *Phil. Trans. R. Soc.* A **215** 253–74
[22] Bragg W L and Bragg W H 1915 *X-Rays and Crystal Structure* (London: G Bell and Sons)
[23] Fewster P F and Andrew N L 1995 *J. Appl. Cryst.* **28** 451–8
[24] Herres N, Obloh H, Bachem K H and Helming K 1999 *Mater. Sci. Eng.* B **59** 202–6
[25] Cullity B D 1956 *Elements of X-Ray Diffraction* (Reading, MA: Addison-Wesley) ch 4, pp 104–37
[26] Reynolds R C Jr 1986 *Clays and Clay Minerals* **34** 359–67
[27] Prince E (ed) 2004 *International Tables for Crystallography* vol C, 3rd edn (Dordrecht: Kluwer) table 6.1.1.4, p 578
[28] Waasmaier D and Kirfel A 1995 *Acta Cryst.* A **51** 416–31
[29] www.ruppweb.org/new_comp/scattering_factors.htm
[30] ESRF, X-ray Oriented Programs (XOP), DABAX library for Cromer Mann coefficients http://www.esrf.eu/Instrumentation/software/data-analysis/xop2.4
[31] Qu B, Zheng X H, Wang Y T, Lin S M, Yang H and Liang J W 2001 *J. Cryst. Growth* **226** 57–61
[32] Tsuchiya H, Sunaba K, Suemasu T and Hasegawa F 1998 *J. Cryst. Growth* **189/190** 395–400
[33] As D J, Richter A, Busch J, Lübbers M, Mimkes J and Lischka K 2000 *Appl. Phys. Lett.* **76** 13–5
[34] Chichibu S F *et al* 2003 *J. Vac. Sci. Technol.* B **21** 1856–62
[35] Lei T, Fanciulli M, Molnar R J, Moustakas T D, Graham R J and Scanlon J 1991 *Appl. Phys. Lett.* **59** 944–6
[36] Cheng T S, Jenkins L C, Hooper S E, Foxon C T, Orton J W and Lacklison D E 1995 *Appl. Phys. Lett.* **66** 1509–11
[37] Fujii K, Kato T, Minegishi T, Yamada T, Yamane H and Yao T 2010 *Electrochemistry* **78** 136–9
[38] Lee S R, West A M, Allerman A A, Waldrip K E, Follstaedt D M, Provencio P P, Koleske D D and Abernathy C R 2005 *Appl. Phys. Lett.* **86** 241904
[39] Srikant V, Speck J S and Clarke D R 1997 *J. Appl. Phys.* **82** 4286–95
[40] Fewster P F 1989 *J. Appl. Cryst.* **22** 64–9
[41] Fewster P F 1996 *Int. School of Crystallography: 23rd Course, X-Ray and Neutron Dynamical Diffraction: Theory and Applications (9–12 April 1996, Erice, Italy)* p 287
[42] Metzger T *et al* 1998 *Phil. Mag.* A **77** 1013–25
[43] Dunn C G and Koch E F 1957 *Acta Metall.* **5** 548–54
[44] Blumenau A T, Elsner J, Jones R, Heggie M I, Öberg S, Frauenheim T and Briddon P R 2000 *J. Phys.: Condens. Matter* **12** 10223–33
[45] Kemper R M, Veit P, Mietze C, Dempewolf A, Wecker T, Bertram F, Christen J, Lindner J K N and As D J 2015 *Phys. Status Solidi* c **12** 469–72
[46] Martinez-Guerrero E *et al* 2002 *J. Appl. Phys.* **91** 4983–7
[47] Sahonta S-L, Frentrup M, Lee L Y, Kappers M J, Oliver R A, Nilsson D, Shaw L J, Ward P J, Humphreys C J and Wallis D J 2016 Phase purity analysis of MOVPE-grown cubic GaN epilayers *Int. Workshop on Nitride semiconductors (IWN 2016) (2–7 October 2016, Orlando, Florida, USA)*
[48] Barchuk M, Holý V, Kriegner D, Stangl J, Schwaiger S and Scholz F 2011 *Phys. Rev.* B **84** 094113
[49] Dupraz M, Beutier G, Rodney D, Mordehai D and Verdier M 2015 *J. Appl. Cryst.* **48** 621–44
[50] Kemper R M *et al* 2012 *Phys. Status Solidi* c **9** 1028–31

[51] Pacheco-Salazar D G, Li S F, Cerdeira F, Meneses E A, Leite J R, Scolfaro L M R, As D J and Lischka K 2005 *J. Cryst. Growth* **284** 379–87
[52] Powell R C, Lee N-E, Kim Y-W and Greene J E 1993 *J. Appl. Phys.* **73** 189–204
[53] Lei T, Moustakas T D, Graham R J, He Y and Berkowitz S J 1992 *J. Appl. Phys.* **71** 4933–43
[54] As D J 2010 Recent developments on non-polar cubic group III nitrides for optoelectronic applications *Proc. SPIE* **7608** 76080G
[55] Rüsing M, Wecker T, Berth G, As D J and Zrenner A 2016 *Phys. Status Solidi* b **253** 778–82
[56] Lischka K 1997 *Phys. Status Solidi* b **202** 673–81
[57] Ayers J E 1995 *J. Appl. Phys.* **78** 3724–6
[58] Romanov A E, Pompe W, Beltz G and Speck J S 1996 *Phys. Status Solidi* b **198** 599–613
[59] Paszkowicz W, Podsiabło S and Minikayev R 2004 *J. Alloys Compd.* **382** 100–6
[60] Strite S, Ruan J, Smith D J, Sariel J, Manning N, Chen H, Choyke W J and Morkoç H 1992 *Bull. Am. Phys. Soc.* **37** 346
[61] Novikov S V, Zainal N, Akimov A V, Staddon C R, Kent A J and Foxon C T 2010 *J. Vac. Sci. Technol.* B **28** C3B1–6
[62] Vurgaftman I and Meyer J R 2003 *J. Appl. Phys.* **94** 3675–96
[63] Dunstan D J 1997 *J. Mater. Sci., Mater. Electron.* **8** 337–75
[64] Roder C, Einfeldt S, Figge S and Hommel D 2005 *Phys. Rev.* B **72** 085218
[65] Wahab Q, Sardela M R Jr, Hultman L, Henry A, Willander M, Jarnzén E and Sundgren J-E 1994 *Appl. Phys. Lett.* **65** 725
[66] La Via F 2012 *Silicon Carbide Epitaxy* (Kerala: Research Signpost)
[67] Okada Y and Tokumaru Y 1984 *J. Appl. Phys.* **56** 314–20
[68] Hoffman R W 1976 *Thin Solid Films* **34** 185–90
[69] Roder C *et al* 2006 *J. Appl. Phys.* **100** 103511
[70] France R M, McMahon W E, Norman A G, Geisz J F and Romero M J 2012 *J. Appl. Phys.* **112** 023520
[71] Sun Y, Li K, Dong J, Zeng X, Yu S, Zhao Y, Zhao C and Yang H 2014 *J. Mater. Sci., Mater. Electron.* **25** 581–5
[72] Chen Y B, Katz M B, Pan X Q, Folkman C M, Das R R and Eom C B 2007 *Appl. Phys. Lett.* **91** 031902
[73] Lee L Y, Frentrup M, Sahonta S-L, Kappers M J, Shaw L J, Ward P J, Nilsson D, Humphreys C J, Oliver R A and Wallis D J 2016 Structural and morphological characterisation of cubic GaN grown on 3C-SiC/Si substrates *Int. Workshop on Nitride Semiconductors (IWN 2016) (2–7 October 2016, Orlando, Florida, USA)*
[74] Inaba K 2014 *Rigaku J.* **30** 7–16